scientific reports

OPEN

The origin and properties of higher-order near- and far-field modes in plasmonic metal nano-rods

Hüseyin U. Tepe

A hydrodynamic model within the discontinuous Galerkin method is used to simulate the non-linear optical properties of plasmonic gold nanorods. Highly pure spherical and vector spherical harmonics are obtained in the near and far-fields, where each over-tone and polarization represents a unique state. The nano-rods may be treated as switchable quasi-atoms, where the activating mechanism is the intense incident pulse. These properties might become useful in future quantum or optical computation applications. The pure harmonical states are explained by the localized Fermi gas pressure gradients, which is the main force driving the second harmonic generation (SHG).

Nonlinear optics is a phenomenon where the induced oscillation moves differently to the intense incident wave. Higher or lower frequency modes arise, where the new frequencies are either integer multiplication, sum, or difference between all modes (both the incident and the subsequently created modes during the non-linear process). Examples of nonlinear optical phenomena are second and third harmonic generation (SHG & THG), where the wave frequency is doubled and tripled, respectively.

Birefringent crystals are commonly used in generating second and third harmonics. The input and output frequencies adhere to phase-matching conditions and the crystal size determines the conversion efficiency[1]. However, phase-matching is not required for nanoparticles[1] as near-fields act as the primary mechanism[2] (different orders of electric modes form during illumination and are localized to the surface of metal nano particles).

Lately, semiconducting nanoparticles have become popular in second and third-harmonic generation studies[3–5] and are resistant to intense irradiation. Silicon and germanium are examples of centrosymmetric lattices, suitable for third harmonic generation at shorter wavelengths (near-IR to UV). While semiconductors are transparent beyond near-infrared wavelengths, gold is excellent at absorbing longer wavelengths. Today's information technology is dependent on the optical single-mode, long-range 1.55 μm band.

Due to its centrosymmetric lattice, bulk gold only supports odd-order nonlinearities (ex. THG). However, within the first two atomic layers at the surfaces, the potential and the electron density profile are non-uniform (spill-out tail)[6–8]. Surfaces allow SHG by breaking the symmetry. SHG is known to stem from bound and free electron contributions[9,10]. A conductive nano-particle is a potential well for its free electrons, generating second-, and higher harmonics under intense source illumination.

Here, the non-linear response of free electrons is modeled and simulated using the Navier–Stokes equation and the discontinuous Galerkin method.

Nano-cylinders with varying tip sharpness are simulated, and their near- and far-field modes are presented. Next, the second-order susceptibility maps are plotted and the microscopic source of SHG is discussed. Finally, dielectric maps, source polarization effects and spectral are compared with expected values.

Methods
Equations and method
Set of hydrodynamic equations
The set of equations constituting the hydrodynamical model is the following:

$$\nabla \times (\nabla \times \vec{E}) + \partial_{tt}\vec{E}/c^2 + \mu_0 \partial_{tt}\vec{P} = 0 \tag{1}$$

$$m_e n \left(\partial_t \vec{v} + (\vec{v} \cdot \nabla)\vec{v} + \gamma\vec{v} \right) = -en \left(\vec{E} + \vec{v} \times \vec{H} \right) - \vec{\nabla}p \tag{2}$$

Micro and Nanotechnology Program, Middle East Technical University, Ankara 06800, Turkey. email: huseyin.tepe1992@gmail.com

$$p = \frac{\hbar^2 (3\pi^2)^{3/2}}{5 m_e} n^{5/3} \tag{3}$$

$$\partial_t n + \nabla \cdot (n\vec{v}) = 0 \tag{4}$$

$$\partial_t \vec{P} = -en\vec{v} \tag{5}$$

, where c is the speed of light, m_e is the electron mass, n is the electron density, γ is the damping parameter ($\gamma_{Au} = 1.075 \cdot 10^{14} s^{-1}$). and p is the quantum pressure of a Fermi gas. The electron velocity $\overrightarrow{\nu}$ is in the Eulerian perspective; the average electron velocity field at a certain point and not the velocity of an individual particle. Equation (1) is the regular wave equation. Equation (2) is the Navier–Stokes equation, driven by the Lorentz and the quantum pressure gradient forces. Equation (2) without the pressure term is, in essence, the Drude model (in the low intensity, linear regime). The classical Drude model fails at nanometer scales as it treats the electrons as non-interacting[11]. Realistically, the electrons do not accumulate on the very ends of nanoparticles under illumination, but spread out on the surface, resulting in a quantum pressure[11]. The polarization density relation (Eq. 5) couples electron densities and velocities with the wave equation (Eq. 1). Equation (4) is the continuity equation. Equation (3) expresses the Fermi gas pressure, which has a nonlinear relation to the electron number density.

The hydrodynamical model together with the standard electromagnetic interface conditions is implemented through the discontinuous Galerkin method in the COMSOL Multiphysics program. The discontinuous elements in a Finite Element Method allow for conforming meshes on rounded objects and account for sharp discontinuities at metal surfaces, without any significant loss of simulation error and stability[11]. Numerous articles have demonstrated the discontinuous FEM method using Maxwell's equations (linear and perturbative nonlinear regime) for photonic applications[12]. The domain is cubical where the side-length of the air-domain and the thickness of the PML layer are 1600 nm. The minimum and maximum mesh element sizes are 4 and 150 nm, respectively. The total simulation time is $1.6 \cdot 10^{-12} s$, and the time step size is $4 \cdot 10^{-16} s$.

Source
The source is a Gaussian pulse, with its polarization along the long axis of the gold nano ellipsoid:

$$\vec{E}_{\text{source}} = (\hat{x} \sin(\theta) + \hat{y} \cos(\theta)) E_0 e^{i\omega t - \alpha(\omega)(t - t')^2} \tag{6}$$

, where ω is the input frequency ($\omega = 1.21 \cdot 10^{15} rad/s$ or $\lambda = 1560 nm$), t' is the offset, a is the pulse width and θ is the polarization angle. The polarization angle is set to 0° for Figs. 1, 2, 3 and 4, and only varied to test the polarization/amplitude dependency of SHG/THG. The second and third harmonic generation is expected to decrease as $\cos^2(\theta)$ and $\cos^3(\theta)$ when angle θ is swept from 0° to 90°, respectively. Localized plasmon lifetimes are generally 100 fs[13] and the pulse length is set to 100 fs. The source pulse amplitude is $E_0 = 10^7$ V/m, far below the melting threshold of gold[14] and similar to commercially available fs pulsed lasers.

Particle dimensions
Five different nano-rods are simulated. The nano-rods include one ellipsoid and four nano-cylinders with different conical tips. Their dimensions and drawings have been added to the supplementary materials. The diameter of all nano-rods is limited to 40 nm, ensuring that the electrons scatter at least once and that the continuum requirement for the hydrodynamical model is retained to a degree (the mean electron scattering length in gold is (37.7–42 nm)[15,16]). The simulation regime is nor fully continuum or free particle, but rather in a transitional regime. At very small scales electrons need to be treated as particles and the semi-classical approach becomes inadequate, necessitating quantum dynamics approaches.

Post-processing
Susceptibility maps
The second-order susceptibility maps are calculated in the post-process. Equation (5) expresses the anisotropic and time-dependent polarization density through electron velocities. Values of $P_i(2\omega)$, $P_i(3\omega)$ and $E_i(\omega)$ are determined by performing a fast Fourier transform (FFT) and extracting the data for the corresponding wavelength. The polarization density, electric fields and the higher-order susceptibilities have the following relation:

$$P_i(2\omega) = \varepsilon_0 \sum_{jk} \chi_{ijk}^{(2)} E_j(\omega) E_k(\omega) \tag{7}$$

$$P_i(3\omega) = \varepsilon_0 \sum_{jkl} \chi_{ijkl}^{(3)} E_j(\omega) E_k(\omega) E_l(\omega) \tag{8}$$

The susceptibilities $x^{(2)}$ and $x^{(3)}$ are tensors, but are set as factors here due to the isotropic and centrosymmetric gold lattice.

Spectral widths
The spectral widths, incident polarization dependency and dielectric values are compared to expected values. Equation (9) expresses the pulse length τ for a Gaussian pulse, which is related to the harmonic order by the
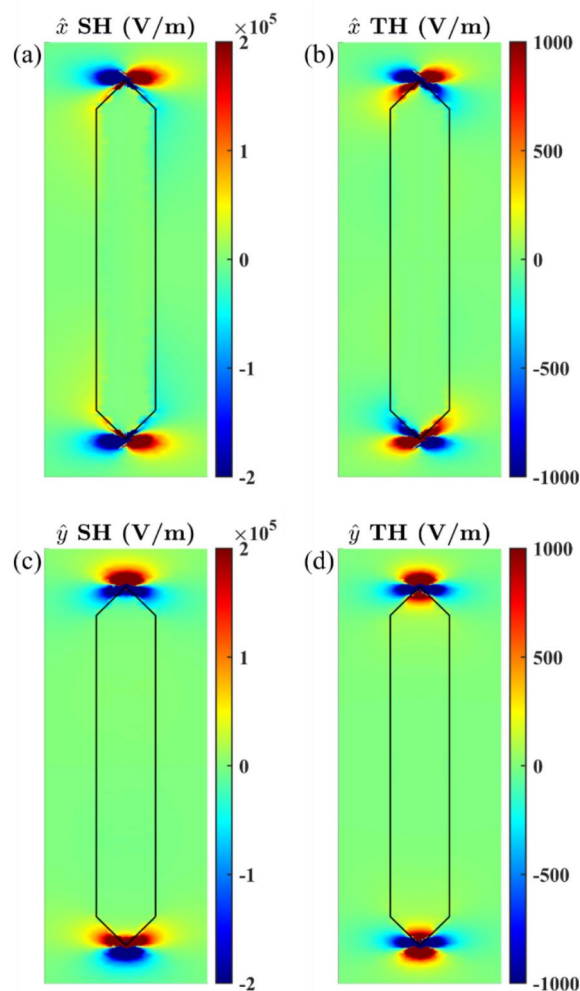
Fig. 1. Nearfield modes of a nano-cylinder with sharp tips. SH/TH are abbreviations for second/third harmonic. The fields are plotted by performing a fast Fourier transform (FFT) on the time-dependent data.

inverse square root. The expected second and third harmonic pulse lengths are 70.7 fs and 57.7 fs, respectively, for a fundamental pulse length of 100.0 fs. The expected values are compared with simulated spectral pulse-widths which are converted to pulse-lengths using Eq. (10), where $\Delta\nu$ is the spectral bandwidth in Hz and the factor of 0.441 is the time-bandwidth product for a Gaussian pulse.

$$\tau = 2\sqrt{\ln(2)}/\sqrt{N \cdot a} \tag{9}$$

$$\tau = 0.441/\Delta\nu \tag{10}$$

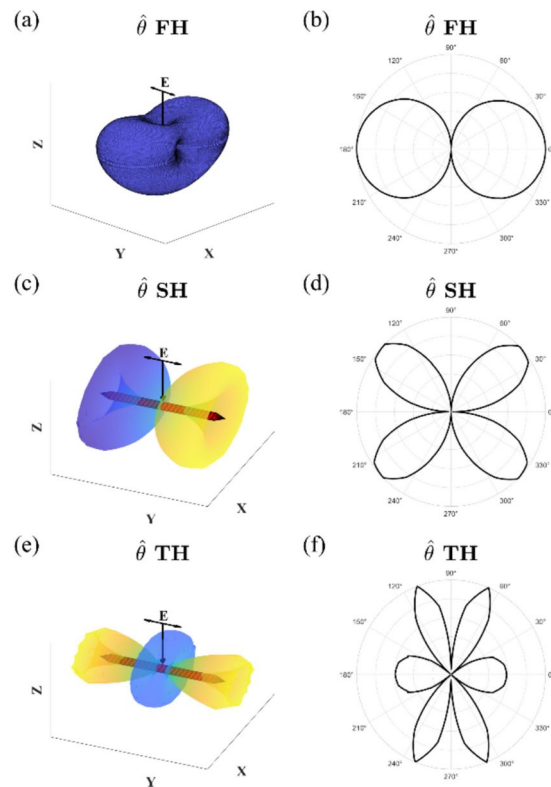*Dielectric map*
The Drude model and Navier–Stokes' equation are similar in the low-intensity (linear) regime and the results are expected to converge. Equation (11) is used to provide a dielectric map of a nano-ellipsoid, which is compared with the theoretical value in Eq. (12).

$$\epsilon = 1 + \frac{\vec{P}(\vec{r})}{\varepsilon_0 \vec{E}(\vec{r})} \tag{11}$$

$$\varepsilon(\omega) = 1 - \frac{ne^2}{\varepsilon_0 m\omega^2} \tag{12}$$

The expected dielectric value at 1560 nm wavelength is -127.1.

Fig. 2. Far-field modes of a nano-cylinder with sharp tips. The second column of figures is the 2D representation of the first 3D column. The $\hat{\theta}$ component curls in the YZ/XZ-plane. FH, SH and TH are abbreviations for first, second and third harmonic. Figure 1(a) uses a different colormap to accentuate the deformed donut shape.
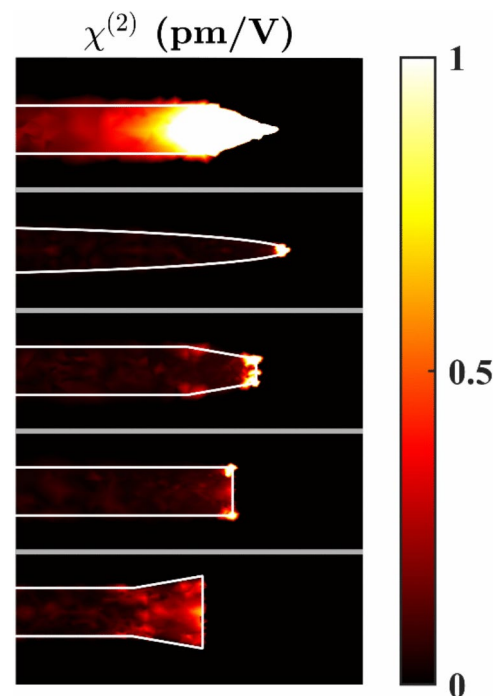
Fig. 3. Second-order susceptibility maps of different nanorods. The peak to lowest values is in descending order and their values are tabulated in Table 1.

4
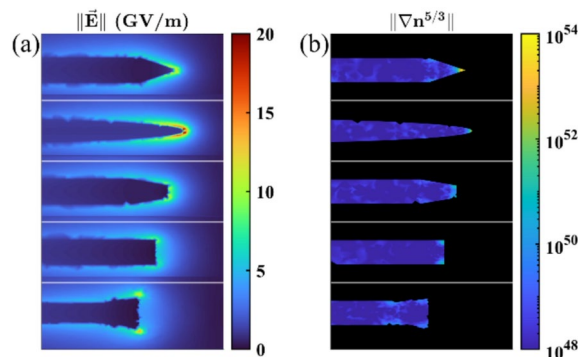
Fig. 4. (**a**) is the plot of the electric field norms and (**b**) is the gradient norm of the quantum pressure p in Eq. (3) without the pre-factor. The maximum values are tabulated in Table 2. The color bar in (**b**) is logarithmic.

Results and discussion
Nearfields
The near- and far-fields (Fig. 1 and 2) consist of highly pure spherical harmonics and vector spherical harmonics, respectively. This is probably the first time pure spherical harmonics have been reported for plasmonic nanoparticles. The results are significant because the near-fields are comparable with the electron wave functions in hydrogen-like atoms and the nano-rods act as switchable quasi-atoms, which could have uses in future quantum or optical computing applications. Each spherical harmonic is orthogonal to one another and unique energy states are formed under intense illumination. The states can be turned on or off by simply turning the illuminating source on or off. Another advantage of nano-particles is the ability to shift the resonance frequencies changing the size and shape during fabrication.

Frazer has previously analytically shown that an infinite series of spherical harmonics are solutions (zero divergence toroidal and poloidal fields) to the incompressible Navier–Stokes equation[17] and the expected solution for a sphere in the perturbative model ($x^{(2)}$ tensor replacing the Navier–Stokes' equation) is a series of spherical and vector spherical harmonics, respectively[18,19].

The solution series is explained by the non-linear Mie theory, where the incident plane wave is expanded in a series of vector spherical harmonics and inserted into the perturbative non-linear polarization density term[20]. However, the situation for sharp features is different to the case of spherical particles. A detailed study follows in the susceptibilities section, where the localized quantum pressure gradient is determined as the critical force driving the SHG. The effective source is not a series of vector spherical harmonics but instead a localized single mode. In the case of Fig. 1, one may expect pure modes.

The finite difference time domain (FDTD) method is another alternative to the discontinuous Galerkin method. Figure 1 is compared with the work of Sukharev et al. who simulated a gold cuboid[21]. The FDTD method yields similar modes, but smeared, whereas the discontinuous Galerkin method localizes the fields to edges and corners. One possible cause might be the implementation of the electromagnetic interface conditions. The discontinuous Galerkin method uses discontinuous shape-functions on a geometry conforming mesh, whereas the FDTD method suffers from staircasing at the boundary (although methods remedying the effects of staircasing exist[22]).

Note that the semi-classical method here assumes a homogeneous ionic background and does not consider atomic effects at the tips, but is valid for nano-antenna pairs and arrays, where the gap exceeds a few nanometers. Quantum dynamics simulation methods are preferable for applications involving very small particles, where the sizes and gaps are approximately (or below) one nanometer. Studies have demonstrated large differences between dipole approximations and quantum dynamics methods at length scales below one nanometer[23], especially when multiple atom clusters in close proximity are involved[24,25].

Far-fields
Figure 2 shows almost pure vector spherical harmonics. The results in Fig. 2b, d and f are common in experimental studies, where the first harmonic radiates two lobes, the second harmonic generation radiates four lobes and the third harmonic generation radiates six lobes (the antenna in the experimental study rests on an opaque substrate)[18,26–28]. It is therefore safe to say that the far-field results are accurate and the nano-rods scatter vector spherical harmonic modes fairly purely. The radiated second and third harmonics are obtained directly and the first harmonic is obtained by subtracting the reference data consisting of an empty air-domain from the non-linear data. The fundamental mode consists of a deformed donut with no front-scattering and higher back-scattering.

Similarly to the results in the previous section, the linear and non-linear Mie theory predicts a series of vector spherical harmonics. However, the higher-harmonics are accelerated by localized quantum pressure gradients.

The scattered field polarization is mostly aligned with the incident wave ($\hat{\theta}$-direction), only having a small cross-talk with the perpendicular $\hat{\varphi}$-component. The radial component is not relevant in the far-field and the $\hat{\varphi}$-component is tiny in comparison (added in the supplementary materials). The average second harmonic

Rods	Max	Mean	Surf. area
Sharp	$2.33 \cdot 10^{-11}$	$6.36 \cdot 10^{-13}$	$5.79 \cdot 10^4$
Ellipsoid	$3.64 \cdot 10^{-12}$	$2.08 \cdot 10^{-14}$	$5.03 \cdot 10^4$
Tapered	$2.36 \cdot 10^{-12}$	$4.54 \cdot 10^{-14}$	$5.83 \cdot 10^4$
Flat	$2.14 \cdot 10^{-12}$	$3.58 \cdot 10^{-14}$	$5.91 \cdot 10^4$
Flanged	$6.96 \cdot 10^{-13}$	$3.06 \cdot 10^{-14}$	$6.02 \cdot 10^4$

Table 1. Average and maximum values of the second-order susceptibilities (m/V) and surface areas (nm²). Types of rods are ellipsoid and cylindrical rods with different tips.

Rods	Max $\left\| \vec{E} \right\|$	Max $\left\| \nabla n^{5/3} \right\|$
Sharp	$1.35 \cdot 10^{10}$	$6.52 \cdot 10^{54}$
Ellipsoid	$2.73 \cdot 10^{10}$	$2.40 \cdot 10^{52}$
Tapered	$1.18 \cdot 10^{10}$	$2.01 \cdot 10^{51}$
Flat	$9.25 \cdot 10^{10}$	$1.94 \cdot 10^{51}$
Flanged	$1.45 \cdot 10^{10}$	$1.00 \cdot 10^{50}$

Table 2. Maximum norm values of the fundamental electric field and the quantum pressure gradient (without its pre-factor). Units are V/m and m⁻⁶.

electric far-field amplitude at a distance of $r = 700$ nm was 26.87 V/m, equating to a radiated power of $2.95 \cdot 10^{-12}$ W. The incident power (assuming an absorption cross-section of $\sigma \approx 3$) is $1.58 \cdot 10^{-12}$ W, leading to a SH power conversion ratio of $\sim 7 \cdot 10^{-10}$.

Susceptibilities

Second-order susceptibilities were calculated using Eqs. (7 and 8) and the maps are presented in Fig. 3. One can observe that the particle shape has a huge impact on SHG. The sharp nano-cylinder has second-order susceptibility over one order of magnitude greater compared to the blunter shapes. Another observation is the non-uniformity of SHG. Contributions come mainly from corners. The peak and average susceptibility values are tabulated in Table 1, and sharper tips are correlated with increased SHG, independent of surface area.

Important to note: the hydrodynamical set of equations is a partial description of SHG. The symmetry breaking surface effect requires an additional microscopic description. The following discussion compares the hydrodynamical results with reported experimental susceptibilities and dissects the SHG contribution to the two components, particle shape and surface area.

Although the non-linear response depends on large electric field amplitudes, it does not explain the large difference in SHG between the nanorods. Figure 4a plots the fundamental electric field norms. The differences between the nanorods are far below one order of magnitude and the ellipsoid has the greatest electric field enhancement. If the non-linearity had purely been driven by Lorentz forces the differences in Fig. 3 would be significantly smaller. Figure 4b plots the map of the quantum pressure gradient (without the pre-factor in Eq. 3) and the difference is between two and four orders of magnitude. The conclusion is: SHG is mainly driven by the electron-density gradient, not the electric field amplitudes. The effects of quantum pressure are known to shift the resonance frequency and were previously suspected as a critical factor in SHG[29,30].

Studies on symmetrical and smooth nano-particles have shown a correlation between particle surface area and second-order hyperpolarizabilities[31,32]. The surface area was the main factor determining the second-order hyperpolarizability and it had a linear dependency. The measured hyperpolarizabilities were on the order of $\beta \sim 10^{-24}$ esu which equate to $x^{(2)} \sim 10^{-13}$ m/V. The hyperpolarizability and second-order susceptibility are related through: $\sqrt{N\beta} = \chi^{(2)}$ (electrostatic units). The number density of nanorods is assumed $N \sim 10^{17}$ cm⁻³ (from TEM images). The reported surface area dependent susceptibility is on average an order of magnitude lower and higher compared to the peak and average values in Table 1, respectively.

So far, non-contributing smooth surfaces have been assumed. But the hydrodynamical model can be used to explain SHG from a rough surface as every defect contributes to SHG[33]. However, symmetry breakage at the surface is not explained, and added roughness requires fine meshing, increasing computation requirements.

Experimental studies on sharp nano prisms show that the increase in corner sharpness increases the hyperpolarizability by 8 times[34]. Triangles with rounded corners had similar SHG properties as spherical particles and the corner sharpness was determined to be the dominating factor (over surface area) in SHG. The authors also performed a hydrodynamical FDTD simulation on nano triangles, showing strong electric fields on the corners. In a different study, the hyperpolarizabilities of tetra-pods (with varying corner sharpness) were determined and the sharpest nano tetra-pods had a hyperpolarizability over 10 times greater compared to nanospheres[35]. The hyperpolarizabilities were sensitive to particle sharpness, decreasing rapidly for blunter tips and plateauing until slowly reaching the hyperpolarizability of spheres.

The hydrodynamical simulations here give peak and average second-order susceptibilities (for the sharp nano-cylinder) over 30 and 20 times greater compared to the flanged nanorod, respectively. The greater difference compared to experimental results is likely due to the perfectly sharp tips in the simulation.

Overall, the hydrodynamical model is able to explain the SHG from sharper features, but unable to explain the symmetry breakage of the air-particle interface[7]. A perturbative surface susceptibility could be added but it would defeat the non-perturbative nature of the hydrodynamical model.

Spectral and dielectric properties

The dielectric function map was obtained using Eq. (11) and compared with an expected theoretical dielectric value from the Drude model. The dielectric values are uniform and range from -127.3 to -127.6 and are close to the Drude value of -127.1 at 1560 nm.

The spectral widths are converted to pulse lengths (fs) using Eq. (10) and are compared with expected values according to Eq. (9). The simulated pulse lengths are 98.8, 70.7 and 57.5 fs for the fundamental, second and third harmonic, respectively. The simulated values are close to the expected values of 100, 70.7 and 57.7 fs.

The incident polarization is varied and non-linear amplitudes are plotted. The fundamental, second and third harmonics have a $\cos(\theta)$, $\cos^2(\theta)$ and $\cos^3(\theta)$ dependency, respectively. The results are according to expectations as the amplitude of the second and third harmonics are quadratically and cubically dependent on the fundamental amplitude.

All figures on dielectric maps, spectra and polarization dependent plots are appended in the supplementary materials.

Conclusions

Highly pure spherical harmonics are simulated at the tips of the nanorods under intense illumination. In analog, highly pure vector spherical harmonics are simulated for the radiated far-fields.

Second-order susceptibility maps are obtained, whose values are directly correlated to the shape of the tips. The critical factor enhancing SHG is the quantum pressure gradient and not the Lorentz force. The hydrodynamic model is accurate in explaining SHG from sharp edges but does not account for symmetry breaking surfaces. Between sharp and blunt tips, a difference of over 30 times is predicted in second-order susceptibility.

Additionally, dielectric maps are obtained and are in agreement with the Drude model. The source polarization is varied and the fundamental, second and third harmonics are shown to depend linearly, quadratically and cubically to cosine. Finally, the spectral widths change as the inverse square root of the harmonic order.

Data availability

References

1. Kauranen, M. & Zayats, A. V. Nonlinear plasmonics. *Nat. Photonics* **6**(11), 739–748. https://doi.org/10.1038/nphoton.2012.244 (2012).
2. Liu, T. et al. Third- and second-harmonic generation in all-dielectric nanostructures: A mini review. *Front. Nanotechnol.* **4**, 891892 (2022).
3. Sederberg, S., Firby, C. J. & Elezzabi, A. Y. Efficient, broadband third-harmonic generation in silicon nanophotonic waveguides spectrally shaped by nonlinear propagation. *Opt. Express* **27**(4), 4990–5004 (2019).
4. Grinblat, G., Li, Y., Nielsen, M. P., Oulton, R. F. & Maier, S. A. Efficient third harmonic generation and nonlinear subwavelength imaging at a higher-order anapole mode in a single germanium nanodisk. *ACS Nano* **11**(1), 953–960. https://doi.org/10.1021/acsnano.6b07568 (2017).
5. Xie, R., He, X., Wang, W., Zheng, L. & Shi, J. Efficient third harmonic generation from magnetic resonance in low-index dielectric nanopillars. *Photonics* **11**(2), 159. https://doi.org/10.3390/photonics11020159 (2024).
6. Khalid, M. & Ciraci, C. Enhancing second-harmonic generation with electron spill-out at metallic surfaces. *Commun. Phys.* **3**(1), 214. https://doi.org/10.1038/s42005-020-00477-0 (2020).
7. Sipe, J. E., So, V. C. Y., Fukui, M. & Stegeman, G. I. Analysis of second-harmonic generation at metal surfaces. *Phys. Rev. B* **21**(10), 4389–4402. https://doi.org/10.1103/PhysRevB.21.4389 (1980).
8. Ashcroft. N. W. Mermin, N. D. Solid State Physics, Belmont, CA: Brooks/Cole, (1976).
9. Scalora, M. et al. Second- and third-harmonic generation in metal-based structures. *Phys. Rev. A* **82**(4), 043828 (2010).
10. Ciraci, C. & De Luca, F. Impact of surface charge depletion on the free electron nonlinear response of heavily doped semiconductors. *Phys. Rev. Lett.* **129**(12), 123902 (2022).
11. Huang, Y., Li, J. & Yang, W. Theoretical and numerical analysis of a non-local dispersion model for light interaction with metallic nanostructures. *Comput. Math. Appl.* **72**(4), 921–932 (2016).
12. Liu, F., Yang, W. & Li, J. A FETD scheme and analysis for photonic crystal waveguides comprising third-order nonlinear and linear materials. *J. Comput. Appl. Math.* **424**, 115005 (2023).
13. Yi, R., Wu, W. & Zhang, X. Femtosecond autocorrelation of localized surface plasmons. *Nanomaterials* **13**(9), 1513. https://doi.org/10.3390/nano13091513 (2023).
14. Ginzburg, P., Krasavin, A. V., Wurtz, G. A. & Zayats, A. V. Nonperturbative hydrodynamic model for multiple harmonics generation in metallic nanostructures. *ACS Photonics* **2**(1), 8–13. https://doi.org/10.1021/ph500362y (2015).
15. Kolwas, K. & Derkachova, A. Damping rates of surface plasmons for particles of size from nano- to micrometers; reduction of the nonradiative decay. *J. Quant. Spectrosc. Radiat. Transfer* **114**, 45–55. https://doi.org/10.1016/j.jqsrt.2012.08.007 (2013).
16. Gall, D. Electron mean free path in elemental metals. *J. Appl. Phys.* **119**(8), 085101. (2016).
17. Frazer, M. C. Spherical harmonic analysis of the Navier-Stokes equation in magnetofluid dynamics. *Phys. Earth Planet. Inter.* **8**(1), 75–82. https://doi.org/10.1016/0031-9201(74)90112-5 (1974).

18. Bernasconi, G. D., Butet, J. & Martin, O. J. F. Mode analysis of second-harmonic generation in plasmonic nanostructures. *J. Opt. Soc. Am. B* **33**(4), 768–779. https://doi.org/10.1364/JOSAB.33.000768 (2016).
19. Butet, J. et al. Multipolar second harmonic generation from metallic nanoparticles. *Metal Nanostruct. Photonics* https://doi.org/10.1016/B978-0-08-102378-5.00006-4 (2019).
20. Butet, J. et al. Nonlinear Mie theory for the second harmonic generation in metallic nanoshells. *J. Opt. Soc. Am. B* **29**(8), 2213–2221 (2012).
21. Li, C. et al. Second harmonic generation from a single plasmonic nanorod strongly coupled to a WSe2 monolayer. *Nano Lett.* **21**(4), 1599–1605 (2021).
22. Dey, S. & Mittra, R. A locally conformal finite-difference time-domain (FDTD) algorithm for modeling three-dimensional perfectly conducting objects. *IEEE Microwave Guided Wave Lett.* **7**(9), 273–275. https://doi.org/10.1109/75.622536 (1997).
23. Khalili, F., Vendrell, O., Hosseini, M. S. & Jamshidi, Z. Quantum dynamics of plasmonic coupling in silver nanoparticle dimers: Enhanced energy and population transfer via emitter interaction. *J. Phys. Chem. Lett.* **16**(10), 2661–2671 (2025).
24. Ilawe, N. V., Oviedo, M. B. & Wong, B. M. Real-time quantum dynamics of long-range electronic excitation transfer in plasmonic nanoantennas. *J. Chem. Theory Comput.* **13**(8), 3442–3454 (2017).
25. Ilawe, N. V., Oviedo, M. B. & Wong, B. M. Effect of quantum tunneling on the efficiency of excitation energy transfer in plasmonic nanoparticle chain waveguides. *J. Mater. Chem. C* **6**(22), 5857–5864 (2018).
26. Maekawa, H. et al. Wavelength and polarization dependence of second-harmonic responses from gold nanocrescent arrays. *J. Phys. Chem. C* **124**(37), 20424–20435 (2020).
27. Sukharev, M., Drobnyh, E. & Pachter, R. Fano plasmonics goes nonlinear. *J. Chem. Phys.* **157**(13), 134105 (2022).
28. Yin, Y., Yao, J., Ye, L., Cai, G. & Liu, Q. H. Tailoring third harmonic generation from anapole mode in a metal-dielectric hybrid nanoantenna. *IEEE Photonics J.* **13**(4), 1–6 (2021).
29. Ciraci, C., Poutrina, E., Scalora, M. & Smith, D. R. Origin of second-harmonic generation enhancement in optical split-ring resonators. *Phys. Rev. B* **85**(20), 201403 (2012).
30. Ciraci, C., Pendry, J. B. & Smith, D. R. Hydrodynamic model for plasmonics: A macroscopic approach to a microscopic problem. *ChemPhysChem* **14**(6), 1109–1116 (2013).
31. Ngo, H. M., Nguyen, P. P. & Ledoux-Rak, I. Optimization of second harmonic generation of gold nanospheres and nanorods in aqueous solution: The dominant role of surface area. *Phys. Chem. Chem. Phys.* **18**(4), 3352–3356. https://doi.org/10.1039/C5CP06850A (2016).
32. Verma, M. S., Kumar, M. & Chandra, M. Controlling second harmonic generation of gold nanorods: Surface area matters more than aspect ratio. *Chem. Phys. Lett.* **741**(16), 137112. https://doi.org/10.1016/j.cplett.2020.137112 (2020).
33. Grynko, Y. et al. *Recent trends in computational photonics* (Springer, 2017).
34. Minh Ngo, H. et al. High yield synthesis and quadratic nonlinearities of gold nanoprisms in solution: The role of corner sharpness. *Israel J. Chem.* **63**(12), e202200009. https://doi.org/10.1002/ijch.202200009 (2023).
35. Lyu, J. et al. Shape-controlled second-harmonic scattering from gold nanotetrapods. *J. Phys. Chem. C* **126**(23), 9831–9835 (2022).

Author contributions
All contributions belong to the corresponding author "Hüseyin U. Tepe".

Funding
I have received no funding.

Declarations

Competing interests
The authors declare no competing interests.

Additional information

Publisher's Note Springer Nature remains neutral with regard to jurisdictional claims in published maps and institutional affiliations.
Publisher's note Springer Nature remains neutral with regard to jurisdictional claims in published maps and institutional affiliations.